geotechnics

Article

# An Analytical Study on Soil Water Index (SWI), Landslide Prediction and Other Related Factors Using XRAIN Data during the July 2018 Heavy Rain Disasters in Hiroshima, Japan

**José Maria dos Santos Rodrigues Neto [1], Netra Prakash Bhandary [2,*] and Yuichi Fujita [3]**

1 Graduate School of Science and Engineering, Ehime University, Matsuyama 790-0825, Japan; rodrigues_neto94@hotmail.com
2 Faculty of Collaborative Regional Innovation, Ehime University, Matsuyama 790-0825, Japan
3 Penta-Ocean Construction Co., Ltd., Tokyo 112-0004, Japan; fjyu1112@gmail.com
* Correspondence: netra@ehime-u.ac.jp

**Abstract:** The rainfall-induced landslide disasters in July 2018 in Southwestern Japan yet again exemplified the severity of slope failure-related damage and the need for improvement of early warning systems. The Japanese Meteorological Agency (JMA) uses a method based on a threshold value of soil water index (SWI), a conceptual measurement that represents saturation of slope soil. The current SWI early warning system uses 60-min rainfall data on a 5-km$^2$ mesh and does not take into consideration other landslide conditioning factors such as slope angle and geology. This study calculates SWI values during the July 2018 disasters in Kure City (Hiroshima Prefecture) using 1-min XRAIN rainfall data in a 250-m mesh to investigate the relationship between SWI and landslide occurrence. It was found that the SWI threshold of 124 mm used in the JMA early warning system for the area was surpassed in all cells. A new SWI threshold calculation method taking slope angle and geology into consideration and produced with machine learning is proposed, comprising power lines for different geological units at a two-dimensional graph where points located above the threshold line represent landslide risk. It is judged that this method would provide a more accurate early warning system for landslide disasters.

**Keywords:** soil water index; landslide prediction; XRAIN data; July 2018 heavy rain disasters in Japan



**Citation:** Rodrigues Neto, J.M.d.S.; Bhandary, N.P.; Fujita, Y. An Analytical Study on Soil Water Index (SWI), Landslide Prediction and Other Related Factors Using XRAIN Data during the July 2018 Heavy Rain Disasters in Hiroshima, Japan. *Geotechnics* **2023**, *3*, 686–699. https://doi.org/10.3390/geotechnics3030037

Academic Editors: Md Rajibul Karim, Md Mizanur Rahman, Khoi Nguyen and Asif Iqbal

Received: 27 June 2023
Revised: 15 July 2023
Accepted: 18 July 2023
Published: 21 July 2023



## 1. Introduction

Landslide-related disasters are the cause of thousands of deaths over the world every year: between 1998 and 2017 more than 4.8 million people were affected by landslides and 28,000 lost their lives due to related phenomena [1]. In Japan, between a similar period of 1999 to the end of 2018 the death toll of landslide-related disasters reached 1242 people [2], which would account for a share of about 4.5% of the world numbers despite Japan's relatively small population and high HDI. Landslide disasters have a few triggering agents including earthquakes or rapid snowmelt, however, the most common one is rainfall occurring either (or both) in high intensity or during a long continuous period, which causes soil to saturate and the respective slope to lose stability [3–5]. Although other preceding factors such as topography, geology or anthropogenic influence also affect landslide probability [5–7], rainfall is still the top trigger for frequent slope failures, which leads to belief that climate change in the near future, with more severe and less predictable rainfall events, will increase the number of landslide-related disasters [8,9].

An example of such a disaster occurred in June–July 2018 in Southwestern Japan when some areas recorded over 1800 mm of rain over 10 days. In the event, one of the most affected towns was Kure City, a port town in Southern Hiroshima Prefecture. Twenty-four fatalities due to landslides were recorded, about 760 buildings were damaged and land transportation lines into and out of the city were cut. Other notorious landslide disasters in Japan include August 2014 in Hiroshima, July 2017 in Northern Kyushu and July 2020 in Kumamoto. It is noted that Japan, being a mountainous island country, is particularly inclined to the scenario of towns cramped between sea and mountains, which offers a high risk of landslide disasters.

Since rainfall is the main trigger for landslide disasters, many previous studies have attempted to use rainfall characteristics such as duration, intensity or cumulative rainfall to assess the climatological conditions necessary for a slope failure to trigger in a specific area, the most popular one being the intensity duration (I-D) threshold, which represents a limit in terms of event rainfall average intensity and duration for landslide activation [5–7,10–12]. The I-D threshold, however, only considers event rainfall, not taking into consideration antecedent rainfall and soil saturation [5].

In an effort to assess rainfall-dependent landslide probability more accurately and to prevent human damage caused by such disasters, one of the strategies used by the Japanese Meteorological Agency (JMA) since 2005 is a localized landslide disaster risk assessment system based on the calculation of soil water index (SWI) derived from antecedent and present rainfall [7,13,14]. Sometimes referred to as soil moisture content, SWI represents the total water depth in the three-tank model, which reflects the saturation level in the soil layers [15,16]. The early warning system used by the JMA, however, uses a relatively wide mesh of 5 km$^2$ and 60-min rainfall data [14], which may be considered too expansive data for landslide assessment calculation. Moreover, there is no system that takes into consideration other landslide pre-conditioning factors such as slope angle or lithology. Although rainfall (and its resultant increase in soil water content) is widely accepted to be the primal trigger for rainfall, it is known that such underlying components are also fundamental for the actual possibility of slope failure occurrence.

One of the recent advances in meteorological monitoring in Japan which may be valuable for landslide hazard assessment is XRAIN (eXtended Radar Information Network), a system of land-based radars that measure real-time precipitation. The system is operated by the Ministry of Land, Infrastructure, Transport and Tourism (MEXT) and its data is made available through the University of Tokyo's Data Integration & Analysis System (DIAS) platform [17]. Different from usual rain gauge station measurement-based data, XRAIN radars acquire precipitation data through bidimensional sampling providing more spatially accurate data, which is vital for the analysis of a local phenomenon such as landslides. Moreover, XRAIN data is readily available in real-time in intervals as short as 1 min.

Yokoe et al., [18], when using XRAIN data to investigate the same July 2018 heavy rain disasters in Southern Hiroshima, evidenced the quantitative accuracy of XRAIN radar data to capture and measure precipitation values in point data, when compared to conventional rain gauge methods, with the exception of rainfall intensity exceeding 80 mm/h. Marc et al. [19] use radar-acquired rainfall data over the landscape of Japan to correlate it with a specific landslide event and discuss how long-term rainfall and event rainfall localization patterns correlate to slope failure occurrence. The authors' evidence that rainfall anomalies in a specific rainfall event are closely relatable to landslide activation, thus evidencing the importance of long-term rainfall analysis. Moriyama & Hirano [20] use XRAIN data to investigate the relationship between maximum three-hour cumulative rainfall and landslide occurrence, evidencing that slope failure activation occurs in peak rainfall timing. Cremonini & Tiranti [21] exemplified a case study of allying radar and gauge rainfall measurement methods in the forecasting and early warning system for landslide disasters, showing that radar data, though susceptible to quantitative error due to miscalibration and other technical difficulties, is viable in the detection of landslide hazards. Other uses of XRAIN include investigation on the development of small-scale guerilla rain clouds [22]; detailed rainfall measurement methods for forecasting [23]; and snowfall precipitation measurement methods [24].

There is still much work to be done in the field of landslide hazard assessment to develop strategies to reduce landslide risk and improve early warning systems, and much potential in relatively recent technologies such as XRAIN data. This study aims to investigate the landslides in July 2018 at Kure City, using XRAIN data to calculate localized SWI values and achieve a further grasp of the dynamic between it and actual landslide occurrence, as well as its relationship with slope angle and lithology, two main landslide pre-conditioning factors. It is expected that the acquired knowledge may contribute to improvement in such SWI-based landslide disaster prediction systems.

## 2. Materials and Methods

### *2.1. Study Area*

The study area of this investigation comprises a rectangular area of 390.5 km$^2$ (approximately 28 km $\times$ 14 km) covering Kure City, south of Hiroshima Prefecture. The cartographical edges that limit the study area are as follows: Top 34.325104 dd; Right: 132.800008 dd; Bottom: 34.197426 dd; Left: 132.500202 dd (Figure 1).

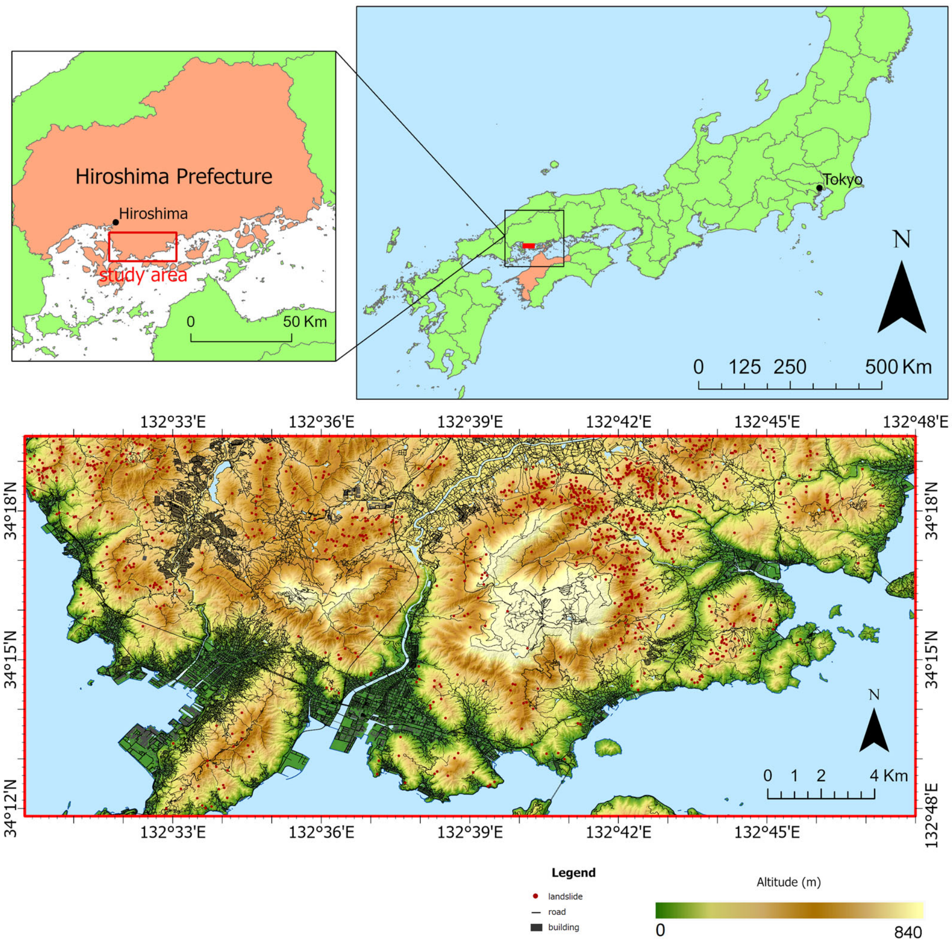


**Figure 1.** Localization map of this study's area, around Kure City, Southern Hiroshima Prefecture, Japan.

Kure is a small port town located between the Seto Inland Sea and the Hiroshima mountains, initially a shipbuilding facility at the end of the 19th century, but soon made into a major dockyard and military base, becoming one of the two main ports of the Imperial Japanese Navy during the World War 2. This situation induced rapid population growth which led to the expansion of the city from the narrow flat terrains of the Kurose River back into the Hiroshima Mountains. As a result, many of the town's habitations are located in or adjacent to rugged terrain. The risks of this scenario, relatively common in the mountainous island country of Japan, were shown in the heavy rain disasters of July 2018 in Southern Hiroshima. Since the area is representative of the high-risk situation of small to medium towns with settlements located near landslide-susceptible rugged terrain in Japan, it was judged that Kure City would be an appropriate study area for this research.

Topographically, the area is mostly comprised of rugged terrain. The altitude varies between sea level around the dockyard areas and 839 m at the peak of Mt. Noro. Other predominant peaks in the area include Mt. Enofuji (664 m), Mt Yasumi (497 m) and Mt. Ege (568 m).

The lithological map used in this study was based on the geological map by by Yamada et al. [25] and is shown in Figure 2. The area's lithological setting is dominated by igneous rocks of the Late Cretaceous, predominantly biotite granite and hornblende-biotite granite of the Hiroshima Granitic Rocks group, commonly referred to by the general term "Hiroshima Granite." In the study area, these rocks are distributed in most of the western portion of the map (Mt. Eboshiwa, Mt. Ege, Mt. Tengujo, Mt. Hachimaki, Mt. Mitsuishi, Mt. Yasumi, Mt. Ichinomatsuko), as well as in a peninsula in the far east of the area (Mt. Mizugaura). Pairing up slightly secondarily to the Hiroshima Granites are the also Late Cretaceous non-alkaline felsic volcanic rocks from the Takada Rhyolites and Hikimi Group, specifically dacite to rhyolite welded tuff, tuffaceous sandstone, mudstone conglomerate, found in the central (Mt. Enofuji, Mt. Hagamine, Mt. Zendana, Mt. Maebira) and the far northeastern part of the area (Mt. Ryume). The southern part of the study area also presents some granodioritic terrains (Mt. Yoshimatsu, Mt. Daikake) and secondarily a melange matrix of the accretionary complex (Mt. Shirataki). In addition, granite porphyry and granophyre dikes of the late cretaceous occasionally cut the Hiroshima Granites (particularly at Mt. Yasumi) rocks in NE-SW orientation, and the granodioritic rocks in NW-SE orientation (around Mt. Daikake). The Quaternary deposits in the area, found along river vales, plains and deltas, comprise sand, mud and gravel from the Saijo Formation, or gravel, sand and mud alluviums from the Holocene.

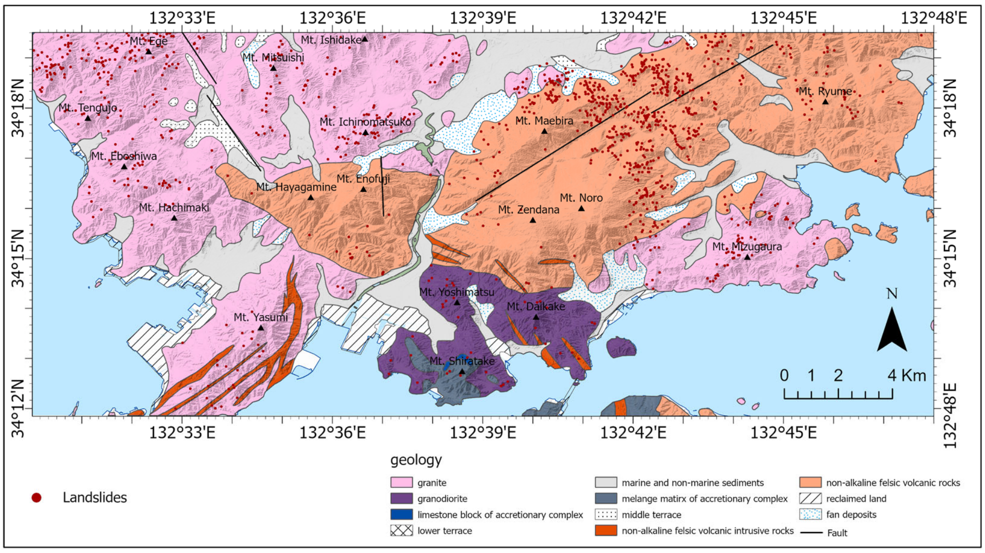

**Figure 2.** Lithological map of the study area based on Yamada et al. [25].

It is well known that the predominant bedrock lithology of the area, coarse biotite granite/granodiorite and hornblende-biotite granite/granodiorite, the "Hiroshima Granites", are very easily weathered, changing into a soil commonly referred to as Masado, or "real sand", in Japanese [26]. Masado granitic soil is known to be extremely permeable and becomes very brittle when wet, characterizing slopes particularly prone to failure during heavy rainfall events.

The GIS data used in the analysis (such as the digital elevation model, landslide points of the July 2018 disasters) were provided by the Geospatial Information Authority of Japan [27], and the geological information is based on the 1:200,000 geological map of Hiroshima by Yamada et al. [25]. The utilized DEM provided by the Geospatial Information

Authority of Japan [27] is acquired with airborne laser survey with 0.2″ interval (5-m resolution) and has 0.3-m vertical accuracy. Although it is arguable that a 1:200,000 geological map would be relatively coarse for a slope failure study, the 1:200,000 map by Yamada et al. [25] was chosen since it encompasses the whole of the study area and is representative of the lithological setting for the needs of a geotechnical approach, separating the major units of the geological context of Kure reflecting landslide occurrences in the July 2018 disasters. The GIS platform used in the analysis was ArcGIS Pro.

### 2.2. XRAIN Rainfall Data

The eXtended RAdar Information Network (XRAIN) is a system operated by the Ministry of Land, Infrastructure, Transport and Tourism in almost all the Japanese territory since 2014. It comprises real-time rainfall intensity data, measured every 1 min by land-based Multi-Parameter (MP) radars. The data comprises instant rainfall intensity measurements and is expressed in 287 × 230 m pixel grids on the unit of mm/h [17].

Although arguably not as quantitatively accurate as regular precipitation measurement methods that utilize traditional rain gauges, the advantage of the use of radars for rainfall intensity observation is that by transmitting radio waves to detect rain clouds over an extensive area, it measures information over an extensive bi-dimensional area, as opposed to the point-based measurement executed with rain gauge stations. Thus, by actually performing data collection over an extended area rather than using extrapolated specific point measurements, radar observation is more spatially reliable for rainfall localization analysis. Moreover, XRAIN's MP radar technology uses multipolarization of vertical and horizontal waves, allowing for more accurate observation.

XRAIN also shows advantages in spatial and time resolution when compared to other conventional weather radars, such as C-band weather radars: XRAIN allows for data collection in 250-m mesh every 1 min, while C-band weather radars gather data in a 1 km mesh every 5 min. In addition, XRAIN data is available for distribution in 1 to 2 min after measurement, while C-band radar data is in 5 to 10 min. This means that XRAIN radars would be able to provide data for warning systems more swiftly.

XRAIN data can be obtained in the Data Integration & Analysis System (DIAS), a dataset platform operated by the University of Tokyo and sponsored by the Ministry of Education, Culture, Sports, Science and Technology (MEXT).

For the study area in this analysis, the XRAIN mesh comprised 5925 pixels converted to GIS visualization in ArcGIS Pro. The 250-m pixel data were acquired directly with XRAIN radars for the center of each pixel with no interpolation.

### 2.3. Soil Water Index (SWI) Calculation

Slope failure triggering is closely related to the content of water in the slope's soil, as it potentially deteriorates its stability, meaning that it is necessary to judge not only the amount of soil water due to present rainfall but also the amount due to past rainfall, and how much of it remains in the soil past a given amount of time. Although it is difficult to measure the actual soil water content in an area, SWI is a model developed to calculate the conceptual soil water content, influenced by recorded hourly precipitation [7].

Sugawara et al. [15] first proposed calculation of SWI using a tank model (Figure 3), where three tanks are placed vertically, and each tank represents a soil layer where moisture content is stored and discharged: the top tank corresponds to the structure of the ground surface and surface runoff; the second tank to the intermediate runoff; and the third tank to the base groundwater runoff. The runoff components for water that flow out of the system are represented by outlets on the side of tanks. The tanks also have infiltration components for water that moves deeper into the tank below it, represented by outlets at the bottom of each tank (except for the third tank, below which an impermeable layer of bedrock is supposed to be located). Consequently, every take has an inflow of water from the tank directly above it, and the top tank has an inflow corresponding to precipitation. The SWI value (correspondent to the soil water content) *SWI* is the total height (in mm) of water remaining in all the tanks at a given time [15,16]:

$$SWI = S_1 + S_2 + S_3, \tag{1}$$

where $S_{1–3}$ is the amount of water remaining in each of the three tanks, calculated through the following formulas:

$$S_1(t + \Delta t) = (1 - \beta_1 \Delta t) \cdot S_1(t) - q_1(t) \cdot \Delta t + R, \tag{2}$$

$$S_2(t + \Delta t) = (1 - \beta_2 \Delta t) \cdot S_2(t) - q_2(t) \cdot \Delta t + \beta_2 \cdot S_1(t) \cdot \Delta t, \tag{3}$$

$$S_3(t + \Delta t) = (1 - \beta_3 \Delta t) \cdot S_3(t) - q_3(t) \cdot \Delta t + \beta_1 \cdot S_2(t) \cdot \Delta t, \tag{4}$$

where $R$ is rainfall, $\beta_{1–3}$ are dimensionless infiltration coefficients for each tank, and $q_{1–3}$ are the runoff components for each tank, calculated by:

$$q_1(t) = \alpha_1 \{S_1(t) - L_1\} + \alpha_2 \{S_1(t) - L_2\}, \tag{5}$$

$$q_2(t) = \alpha_3 \{S_2(t) - L_3\} \tag{6}$$

$$q_3(t) = \alpha_4 \{S_3(t) - L_4\} \tag{7}$$

where $\alpha_{1–4}$ are dimensionless outflow coefficients for each runoff outlet, and $L_{1–4}$ is the height of each runoff outlet from the base of its respective tank [15,16]. The parameters for Equations (2)–(7) used were the ones proposed by Ishihara & Kobatake [16], which are optimized for granite soil in Japan. These are presented in Table 1.

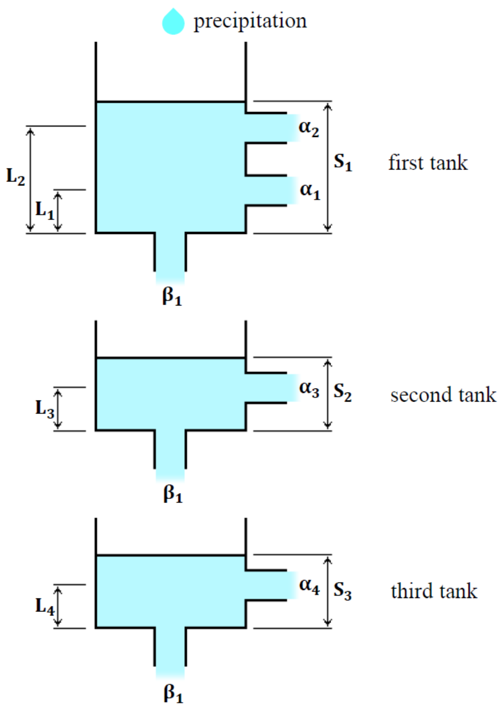


**Figure 3.** Illustration of the tank model used to calculate SWI, as proposed by [15].

**Table 1.** Parameters for SWI calculations optimized for granite soil in Japan, proposed by [16].

| | 1st Tank | 2nd Tank | 3rd Tank |
|---|---|---|---|
| Outlet height (mm) | L1 = 15<br>L2 = 60 | L3 = 15 | L4 = 615 |
| Runoff coefficient (1/h) | α1 = 0.1<br>α2 = 0.15 | α3 = 0.05 | α4 = 0.01 |
| Infiltration coefficient (1/h) | β1 = 0.12 | β1 = 0.05 | β1 = 0.01 |

Sugawara et al. [15] assert that the tank model presents many good points for soil water content analysis, such as being able to reasonably represent the actual physical form of zonal structure groundwater despite its simple form, representing the non-linear characteristic of surface runoff and its several components.

Although originally designed for river discharge analysis and warning systems, SWI calculation is also used for the case of soil water content in failure-prone slopes and consequent landslide disasters [7,14,16,28]. In Japan, the government uses SWI calculations along 60-min cumulative rainfall for a nationwide early-warning system for landslide disasters since March 2007. The system uses Radial Basis Function Network methods to analyze past records of SWI values and occurrence or non-occurrence of landslides, determining the lowest limit of SWI, known as the critical line, above which landslide occurrence is considered likely, and thus evacuation is advised [14]. These values are distributed in a 1-km mesh all throughout the Japanese territory and are found on the JMA website [28]. The critical SWI value for the study area of this research, at the time of the July 2018 disasters, was 124 mm.

## 3. Results

### *3.1. SWI and Slope Failure*

The calculation of SWI values based on cumulative rainfall of the disasters in July 2018 using XRAIN rainfall data showed that the average SWI value for all cells of the study area was 218.2 mm, with most cells between the range of 200–230 mm (Figure 4). It was noted that between those landslide cells, the range with the highest landslide activity was in the range of 210–220 mm, with 81 occurrences (Figure 5).

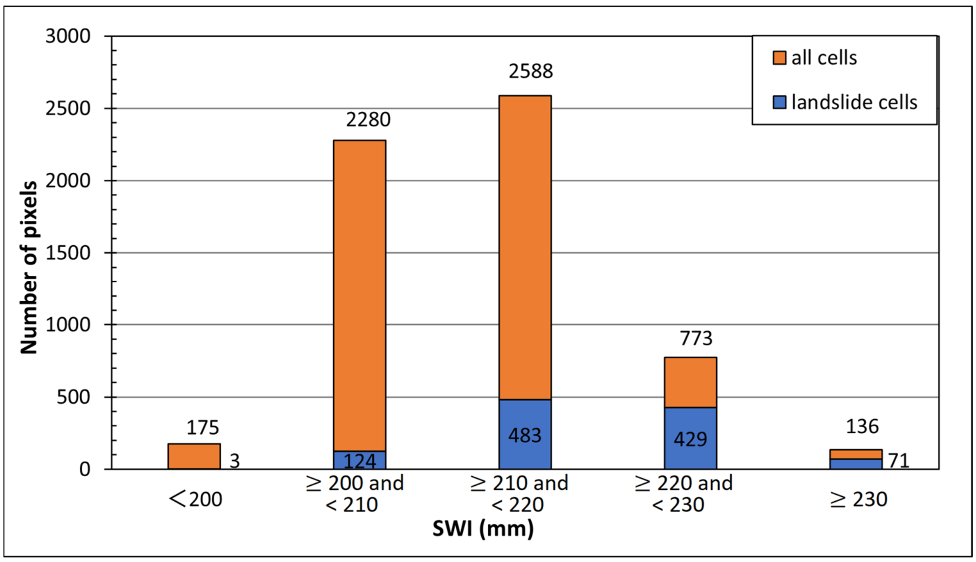


**Figure 4.** Distribution of landslide cells (blue columns) in comparison to all cells (orange columns) according to SWI range. It was noticed that most landslide cells are concentrated between 210 mm and 230 mm SWI.

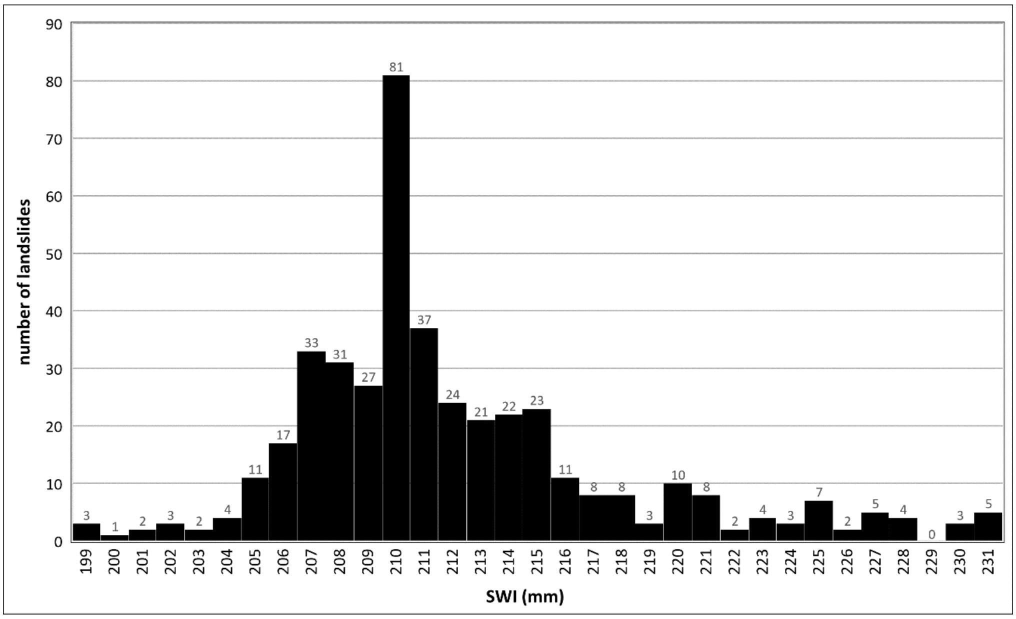


**Figure 5.** Landslide activity per SWI range in landslide cells of the study area. A particularly prominent peak was noticed at the 210 mm range, with 81 landslides.

SWI value distribution in the study area is shown in map form in Figure 6. Higher SWI values seem to be concentrated in the central east region of the study area, specifically at the northeastern face of Mt. Noro. This region is also notable for the high concentration of slope failure points in the July 2018 disasters. When investigating the relationship between SWI range and landslide density in the area, a direct relationship was noticed where higher SWI values lead to higher landslide density (Figure 7).

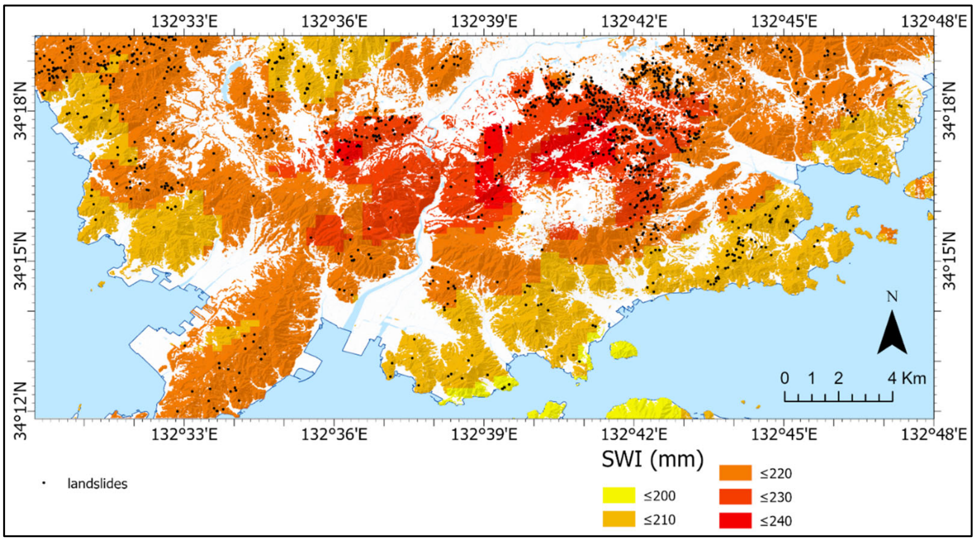


**Figure 6.** Distribution of calculated SWI values for the study area.

Although it was noticed that the landslide early-warning disaster critical value of 124 mm established for the area by the JMA (2023) was exceeded in all points where landslide occurrence was recorded in the study area, that is also true for the whole of the study area: the lowest calculated SWI value was 198 mm.

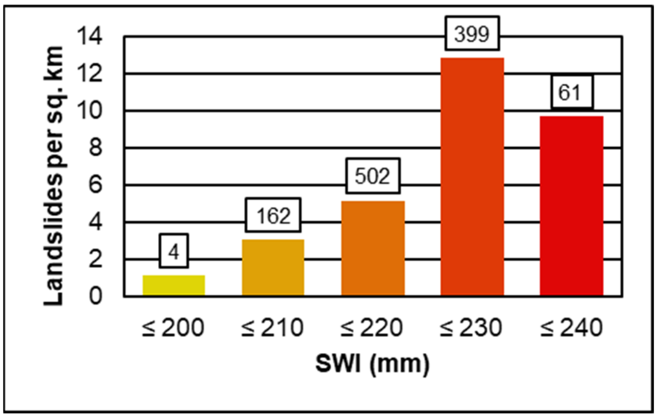


**Figure 7.** Relationship between landslide density and SWI. Values above bars indicate the total number of landslides in the respective SWI range.

### 3.2. SWI and Slope Angle

Only areas with slopes between 20 degrees and 50 degrees were considered for analysis since slope failure probability is not considered significant for slopes outside the range. A map showing the distribution of slope angle in the study area along with landslide cells is shown in Figure 8. Slope failure becomes more common as slope angle increases, reaching peak occurrence between 30 and 35 degrees. Slopes with steeper angles, however, show lower slope failure occurrence (Figure 9).

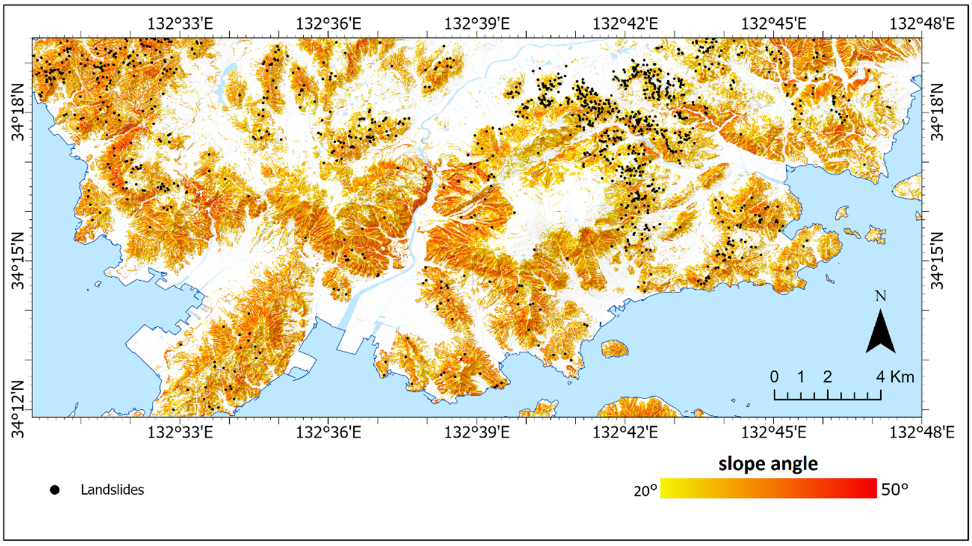


**Figure 8.** Slope failure and landslide cells in the study area. Peak landslide occurrence is recorded in slopes between 30 and 35 degrees.

When comparing landslide cells' SWI value and slope angle, it was noticed that a slight inverse proportional relationship is present, where cells of slopes with steeper angles present lower SWI values. As seen in Figure 9, slope failures occurring in the range between 20 and 25 degrees present an average SWI of 220 mm, while failures occurring in slopes between 45 and 50 degrees present an average SWI of 215 mm.

### 3.3. SWI and Geology

Concerning the distribution of SWI values in terms of the two main geological units of the area, the Hiroshima Granites and the Hikimi Group volcanic rocks, it was noticed that slope failure cells in granitic terrains present an average SWI value of 213 mm, while slope failure cells in volcanic rock terrains have an average SWI value of 222 mm. The fact that slope failures in granitic rock terrains were activated in SWI values generally lower than the slope failures in volcanic rock terrains suggest that granitic terrains are more prone to slope failures.

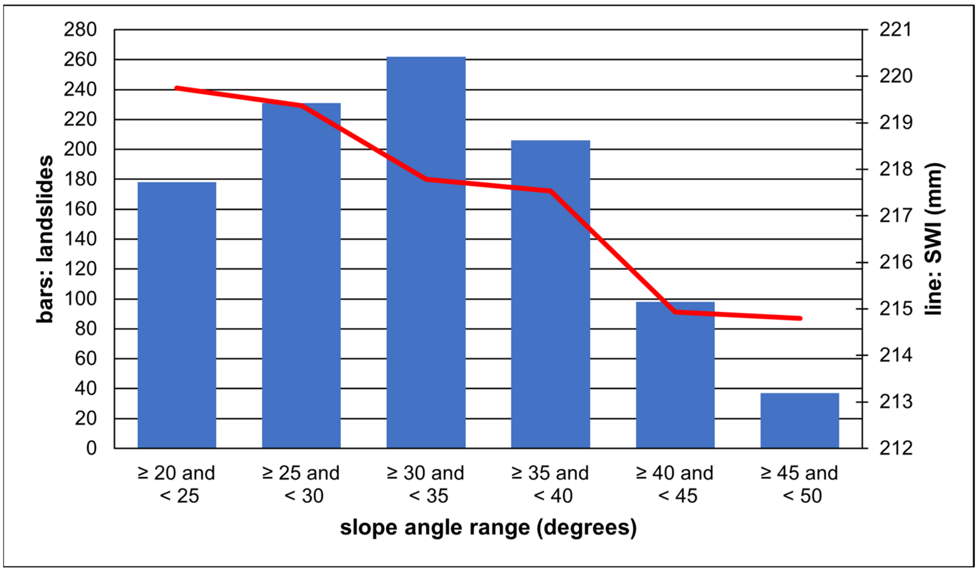


**Figure 9.** Graph illustrating the relationship between SWI (line) and number of landslides (bars) for each slope angle range in landslide cells.

### *3.4. SWI, Slope Angle and Geology Joint Analysis*

The relationship between SWI, slope angle and landslide density in landslide cells for both volcanic and granitic terrains is shown in table form in Figure 10, and in the cartesian graph in Figure 11. It is noticed that the aspect of landslide activation in decreasing slope angles for higher SWI values is more accentuated in granitic rocks, though still present in volcanic rocks as well. It is noticed that both cases exhibit landslide activity increasing with higher SWI values.

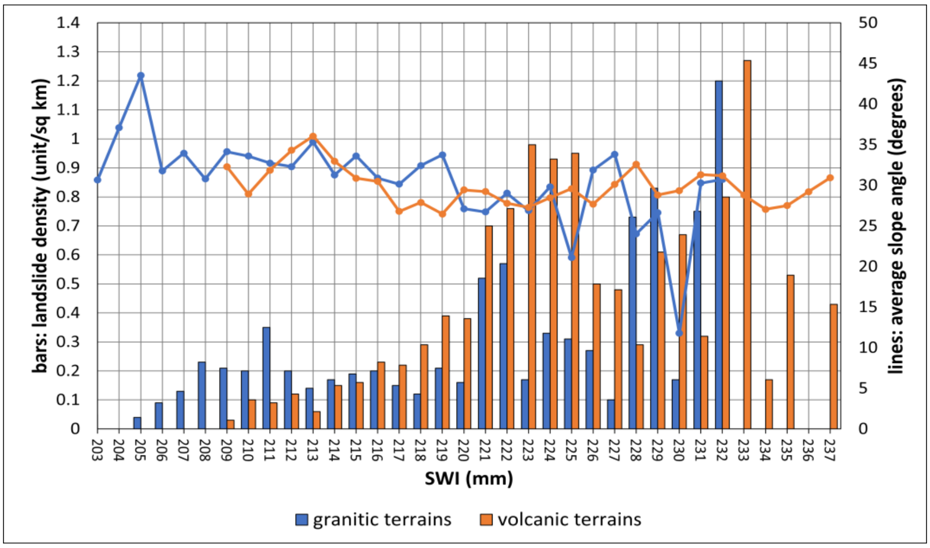


**Figure 10.** Relationship between SWI, slope angle and landslide density in landslide cells for granitic and volcanic terrains of the study area. In granitic terrains, the decreasing slope angle for higher SWI values is well noted, as well as the increasing landslide activity. In volcanic terrains, although increasing landslide activity for higher SWI values is noticed, decreasing slope angle is not as well noticed as in granitic terrains.

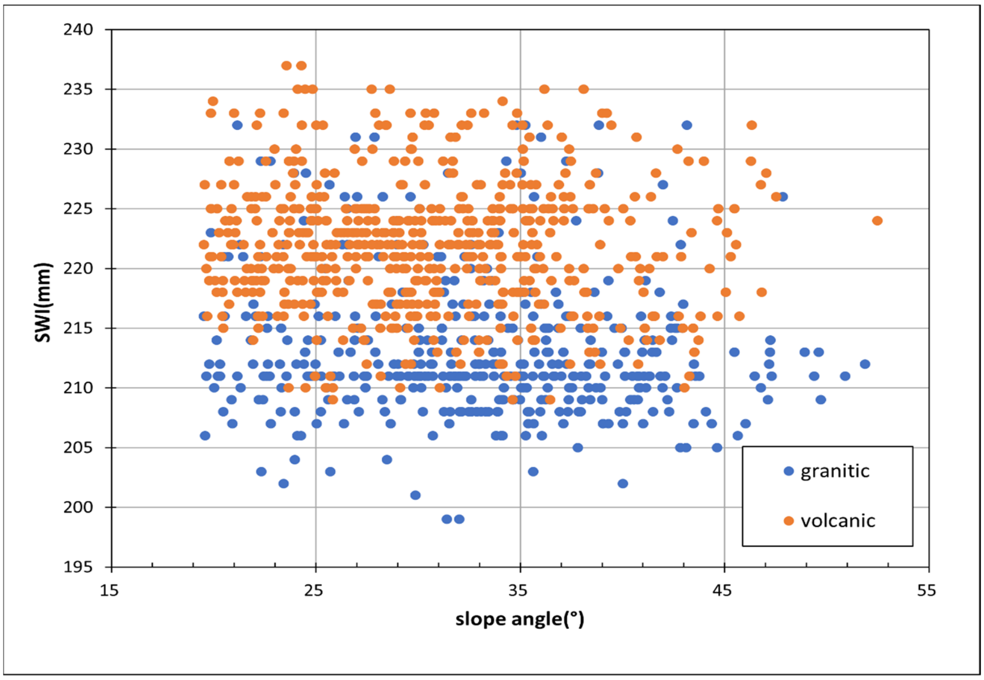


**Figure 11.** Slope failure occurrences in granitic terrains (blue dots) and volcanic terrains (orange dots) in the study area in terms of SWI and slope failure. It is noticeable that landslides in granitic terrains occur in lower SWI values, suggesting that those terrains are more susceptible to slope failure occurrence even with lower rainfall events when compared to volcanic terrains. Slope angle also seems to decrease in higher SWI values.

## 4. Discussion

The higher concentration of landslides in areas related to higher SWI values corroborates the assumption that SWI is an indicator of slope failure susceptibility, as it indicates the concentration of water content inside the soil, a lead trigger for the failure of stability in a slope. This corroborates with the decision by the JMA to determine landslide risk for the nationwide early-warning system based on SWI values, as is also shown in the study area by the fact that all landslide cells surpassed the SWI limit of 124 mm established for the landslide early warning system in the area. It is noted, however, that many cells that recorded no slope failure also surpassed that 124 mm limit, suggesting that the system has an extremely high false positive rate, at least for the study area.

It is judged that one of the strategies to overcome the false positive rate issue would be to base the slope failure SWI threshold allied to other landslide-related factors, such as slope angle and geology, which, as pointed out in the results section of this research, do seem to interfere in the SWI slope failure triggering limit.

Slope angle is commonly known to be a major factor in slope stability, where steeper slopes are generally more prone to failure, up to a certain point. As expected, this dynamic is also observed in the study area regarding the July 2018 disasters, where steeper slopes show higher landslide point density, peaking in the range between 30 and 35 degrees, after which the landslide activity drops considerably. It is judged that this happens because slopes with very steep angles do not contain much remaining landslide-prone soil material, mostly comprised of hard rock and relatively stable cliffs.

As slope angle is one of the determining factors for slope failure susceptibility, it is expected that the SWI threshold would fluctuate depending on the angle of the slope in question. This hypothesis is observed in the results of this research, where landslides occurring in gentler slopes (20 to 25 degrees) require higher SWI values (average 220 mm) to trigger failure, while steeper slopes (40 to 45 degrees) required lower SWI values (average 215 mm). Although there is a difference of only 5 mm in SWI, the pattern is acknowledged and thus it is judged that slope angle data may be used to acquire further accurate SWI thresholds.

Similarly, it was noticed that SWI thresholds also seem to vary according to the respective geology of failure cells. Slope failure occurring in Hiroshima Granite terrains generally shows lower SWI values (average of 213 mm) than those occurring in Hikimi Group volcanic rock terrains (average of 222 mm). The 9 mm SWI disparity may be considered substantial in such a relatively small-scale area, more even than the slope angle.

A proposition, then, would be to use such landslide-conditioning factors (other than SWI) to improve the accuracy of the SWI threshold value. This would mean that the threshold values would not be one-dimensional fixed values, but rather be illustrated in a two-dimensional graph where SWI is represented by a vertical axis and another quantitative factor (e.g., slope angle) would be de-represented by a horizontal axis. The threshold for landslide activation, then, would be a curve along the graph, above which landslides are considered probable. SWI values for areas with different qualitative factors (e.g., geology) would have different curves, since the recorded landslide points would be located more above or below areas respective to other qualitative factors, given that these do differ on landslide probability.

One of the proposed methods for the construction of such threshold lines is by using machine learning technology. In this study, scikit-learn's ensemble random forest algorithm [29] was used by inputting the plotted actual landslide points (in terms of SWI value and slope angle) from the July 2018 disasters as input training data, allowing for the machine learning algorithm to predict in what slope angles would new landslides occur depending on SWI value. A power equation line was then derived with the predicted points, which is used as a proposed threshold line for landslide triggering according to SWI and slope angle. The resultant threshold lines plotted in cartesian coordinates along with the actual landslide points of the July 2018 disasters are shown in Figure 12. Two threshold lines were constructed independently for granitic terrains, represented by the power equation $y = 255.16\ x^{-0.051}$, and for volcanic terrains, with a power equation of $y = 245.7\ x^{-0.033}$, slightly above the volcanic terrain line.

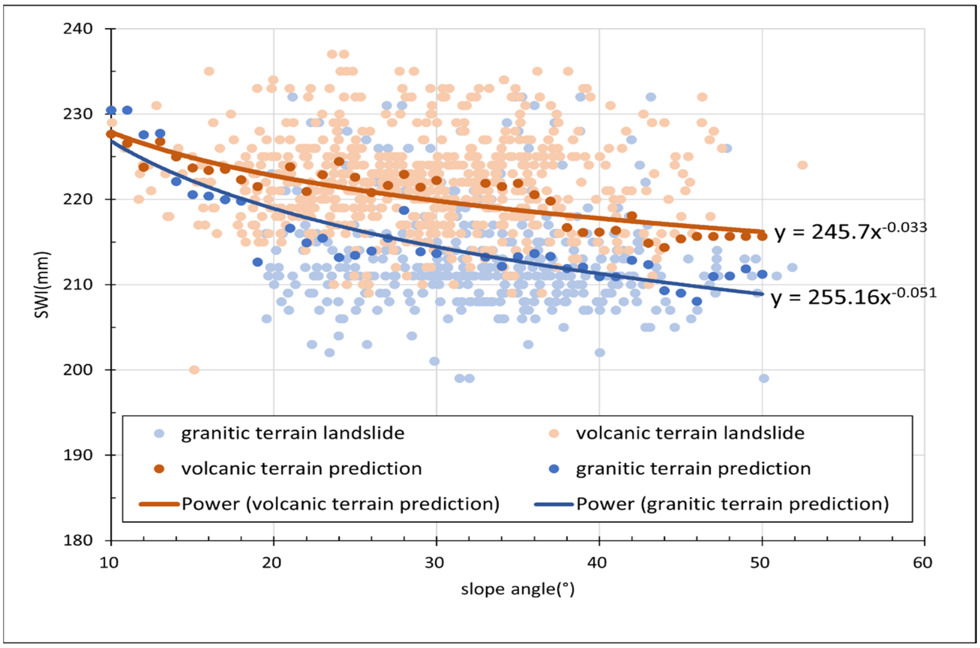


**Figure 12.** Proposed SWI threshold line calculation method taking slope angle and geology into consideration, acquired through inputting actual landslide points' SWI and slope angle values for granitic and volcanic rocks in scikit-learn's ensemble random forest regressor machine learning algorithm, predicting landslide occurrences according to SWI range and deriving a power equation trendline.

Although the use of an early warning system based on precise SWI threshold values differing in small scales depending on the newly inserted factors would arguably be much more complicated and difficult to put into practical use than the current municipality-based one-dimensional threshold warning system, it may be considered that such an improvement in the calculation would provide for more trustworthy warning systems, leading to strategies that would help to prevent damage such as the one seen during the July 2018 disasters.

## 5. Conclusions

SWI is an objective and efficient way to measure slope failure's most common triggering factor, rainfall, in the soil of a given area. It is known, however, that a specific area's landslide susceptibility may vary depending on other underlying landslide-conditioning factors. This study's results demonstrate that small-scale changes in such factors, namely slope angle and geology, seem to critically influence slope failure susceptibility, thus possibly shifting also the SWI threshold value beyond which slope failure is triggered. It is therefore suggested that using both slope angle and geology data as accessory determiners in SWI threshold value for slope failure triggering would improve early-warning systems, currently based solely on SWI value for large-scale areas. The new SWI threshold calculation, acquired through the machine learning technique random forest regressor algorithm, would result in a two-dimensional graph where points located above the threshold curve would represent landslide possibility.

This study proposes a new method and proves its applicability in the current study of Kure City only. Implementation attempts in areas with different settings would be necessary to verify if the model has extensive application potential. Although more complicated than the currently easily applicable municipality-based one-dimensional SWI threshold early warning system, the insertion of other relevant landslide conditioning factors, such as slope angle and geology, would greatly improve the accuracy of early warning systems.

Future studies on this topic could include applying the technique to other areas affected by landslide disasters, as well as investigating the dynamic between SWI and landslide conditioning factors other than slope angle and geology.

**Author Contributions:** J.M.d.S.R.N. and Y.F. conducted all data analysis while the first draft of the manuscript was prepared by J.M.d.S.R.N. and N.P.B. supervised the whole work and made the final check and helped bring the manuscript into submittable format and structure. N.P.B. also suggested J.M.d.S.R.N. and Y.F. to do necessary data analysis and prepare the manuscript text, necessary figures, and tabulated data. All authors have read and agreed to the published version of the manuscript.

**Funding:** This research received no external funding.

**Data Availability Statement:** Publicly available datasets were analyzed in this study. This data can be found on: https://diasjp.net (XRAIN data); https://www.gsi.go.jp/top.html (other GIS data).

**Acknowledgments:** The immensely valuable free access to XRAIN data, widely utilized as a main item in this research, was kindly permitted to by the Data Integration and Analysis System (DIAS) office, from The University of Tokyo.

**Conflicts of Interest:** The authors declare no conflict of interest.

## References

1. United Nations Office for Disaster Risk Reduction. Economic Losses, Poverty and Disasters 1998–2017. Available online: https://www.who.int/health-topics/landslides (accessed on 10 June 2022).
2. Ushiyama, M.; Honma, M.; Yokomaku, S.; Sugimura, K. Characteristics of victims caused by heavy rainfall disasters in July, 2018. *J. Jpn. Soc. Nat. Disaster Sci.* **2019**, *38*, 29–54.
3. Keefer, D. Landslides caused by earthquakes. *Geol. Soc. Am. Bull.* **1984**, *95*, 406–421. [CrossRef]
4. Guzzetti, F.; Malamud, B.D.; Turcotte, D.L.; Reichenbach, P. Power-law correlations of landslide areas in central Italy. *Earth Planet. Sci. Lett.* **2002**, *195*, 169–183. [CrossRef]
5. Chen, C.W.; Saito, H.; Oguchi, T. Analyzing rainfall-induced mass movements in Taiwan using the soil water index. *Landslides* **2017**, *14*, 1031–1041. [CrossRef]

6. Glade, T.; Crozier, M.; Smith, P. Applying probability determination to refine landslide-triggering rainfall thresholds using an empirical Bantecedent daily rainfall model. *Pure Appl. Geophys.* **2000**, *157*, 1059–1079. [CrossRef]
7. Saito, H.; Nakayama, D.; Matsuyama, H. Two Types of Rainfall Conditions Associated with Shallow Landslide Initiation in Japan as Revealed by Normalized Soil Water Index. *SOLA* **2010**, *6*, 57–60. [CrossRef]
8. Gariano, S.; Guzzetti, F. Landslides in a changing climate. *Earth-Sci. Rev.* **2016**, *162*, 227–252. [CrossRef]
9. Lin, Q.; Steger, S.; Pittore, M.; Zhang, J.; Wang, L.; Jiang, T.; Wang, Y. Evaluation of potential changes in landslide susceptibility and landslide occurrence frequency in China under climate change. *Sci. Total Environ.* **2022**, *850*, 158049. [CrossRef]
10. Caine, N. The rainfall intensity–duration control of shallow landslides and debris flows. *Geogr. Ann. A* **1980**, *62*, 23–27.
11. Guzzetti, F.; Peruccacci, S.; Rossi, M.; Stark, C.P. Rainfall thresholds for the initiation of landslides in central and southern Europe. *Meteorol. Atmos. Phys.* **2007**, *98*, 239–267. [CrossRef]
12. Rosi, A.; Peternel, T.; Jemec-Auflič, M.; Komac, M.; Segoni, S.; Casagli, N. Rainfall thresholds for rainfall-induced landslides in Slovenia. *Landslides* **2016**, *13*, 1571–1577. [CrossRef]
13. Okada, K. Soil water index. *Sokkoujihou* **2005**, *69*, 67–100. (In Japanese)
14. Osanai, N.; Shimizu, T.; Kuramoto, K.; Kojima, S.; Noro, T. Japanese early-warning for debris flows and slope failures using rainfall indices with Radial Basis Function Network. *Landslides* **2010**, *7*, 325–338. [CrossRef]
15. Sugawara, M.; Ozaki, E.; Watanabe, I.; Katsuyama, Y. Tank model and its application to Bird Creek, Wollombi Brook, Bikin River, Kitsu River, Sanaga River and Nam Mune. *Res. Note Natl. Res. Cent. Disaster Prev.* **1974**, *11*, 1–64.
16. Ishihara, Y.; Kobatake, S. Runoff Model for Flood Forecasting. *Bull. Disaster Prev. Res. Inst.* **1979**, *29*, 27–43.
17. Data Integration & Analysis System. XRAIN Realtime Precipitation Data. The University of Tokyo, Sponsored by the Ministry of Education, Culture, Sports, Science and Technology. Available online: https://diasjp.net (accessed on 12 June 2022).
18. Yokoe, Y.; Kita, M.; Uchida, T.; Kawahara, Y. Characteristics of precipitation system in hiroshima prefecture during the heavy rainfall event of July 2018 observed using xrain data. *J. JSCE* **2021**, *9*, 212–220. [CrossRef]
19. Marc, O.; Gosset, M.; Saito, H.; Uchida, T.; Malet, J. Spatial Patterns of Storm-Induced Landslides and Their Relation to Rainfall Anomaly Maps. *Geophys. Res. Lett.* **2019**, *46*, 11167–11177. [CrossRef]
20. Moriyama, T.; Hirano, M. Relationship between maximum three-hour cumulative rainfall and landslide area. In Proceedings of the 21st IAHR-APD Congress 2018, Yogyakarta, Indonesia, 2–5 September 2018.
21. Cremonini, R.; Tiranti, D. The Weather Radar Observations Applied to Shallow Landslides Prediction: A Case Study from North-Western Italy. *Front. Earth Sci.* **2018**, *6*, 134. [CrossRef]
22. Harjupa, W.; Nakakita, E.; Sumida, Y.; Yamaguchi, K. Fundamental investigation of generation of guerilla-heavy rainfall using himawari-8 and xrain information in kinki region. *J. Jpn. Soc. Civ. Eng. Ser. B1 (Hydraul. Eng.)* **2018**, *74*, I_283–I_288. [CrossRef]
23. Tsuchiya, S.; Kawasaki, M.; Godo, H. Improvement of the radar rainfall accuracy of xrain by modifying of rainfall attenuation correction and compositing radar rainfall. *Hydraul. Eng. Pap.* **2015**, *59*, I_457–I_462.
24. Masuda, Y.; Itado, M.; Taniguchi, K.; Sakai, K.; Ueda, H.; Yamashita, K.; Nakai, S. Improving of winter quantitative precipitation using XRAIN. *Hydraul. Eng. Pap.* **2018**, *62*. [CrossRef]
25. Yamada, N.; Higashimoto, S.; Mizuno, K.; Hiroshima, T.; Suda, Y. Hiroshima 1:200,000 Geological Map, NI-53-33. Geological Survey of Japan. 1986. Available online: https://www.gsj.jp/Map/JP/docs/200k_doc/ni53_33.htm (accessed on 13 June 2022).
26. Wang, F.; Wu, Y.-H.; Yang, H.; Tanida, Y.; Kamei, A. Preliminary investigation of the 20 August 2014 debris flows triggered by a severe rainstorm in Hiroshima City, Japan. *Geoenviron. Disasters* **2015**, *2*, 17. [CrossRef]
27. Geospatial Information Authority of Japan. Database. Available online: https://www.gsi.go.jp/top.html (accessed on 13 June 2022).
28. Matsuyama, H.; Saito, H.; Zemtsov, V. Application of Soil Water Index to landslide prediction in snowy regions: Sensitivity analysis in Japan and preliminary results from Tomsk, Russia. *Prog. Earth Planet. Sci.* **2021**, *8*, 17. [CrossRef]
29. Pedregosa, F.; Varoquaux, G.; Gramfort, A.; Michel, V.; Thirion, B.; Grisel, O.; Blondel, M.; Prettenhofer, R.W.; Dubourg, V.; Vanderplas, J.; et al. Scikit-learn: Machine Learning in Python. *JMLR* **2011**, *12*, 2825–2830.